EDZ Formation and Associated Hydromechanical Behaviour around ED-B Tunnel: A Numerical Study based on a Two-Part Hooke's Model (TPHM)

Lianchong Li* and Hui-Hai Liu**

···

Abstract

The accuracy in modeling coupled processes in a clay/shale repository is largely determined by the validity of the constitutive relationships and related parameter values. As an attempt to more accurately model the Excavation Damaged Zone (EDZ) formation and associated hydromechanical behavior induced by excavation in clay/shale, a recently developed stress-strain relationship (a two-part Hooke's model, abbreviated as TPHM) and associated formulations regarding rock hydraulic/mechanical properties were incorporated and implemented in FLAC3D in detail. TPHM is based on a macroscopic-scale approximation using a natural-strain-based Hooke's law to describe elastic deformation for a fraction of pores subject to a large degree of deformation; an engineering-strain-based Hooke's law is used for the other part. The usefulness and validity of the TPHM and associated formulations are demonstrated by the consistency between simulation results and field observations from the ED-B tunnel at the Mont Terri site. The simulation results, which are sensitive to the constitutive relationships used in the model, capture both the observed displacements and the size of the damage zone, whereas the approach based on the conventional Hooke's law underestimates both. The fracture modeling provide insight into the evolution of fractured zone that are impossible to be observed in field and are difficult to be considered with static stress analysis approaches.

Keywords: *numerical simulation, failure process, constitutive model, excavation damaged zone, heterogeneity*

···

1. Introduction

Clay/shale has been considered as potential host rock for geological disposal of high-level radioactive waste throughout the world, because of its low permeability, low diffusion coefficient, high retention capacity for radionuclides, and capability to self-seal fractures. Coupled Thermal, Hydrological, Mechanical, and Chemical (THMC) processes are expected to have a significant impact on the long-term safety of a clay repository (Kim *et al*., 2011). For example, the excavation damaged zone (EDZ, the EDZ is also sometimes referred as the "Disturbed Rock Zone" (DRZ)) near repository tunnels can modify local permeability (resulting from induced fractures), potentially leading to less confinement capability (Stormont, 1997; Tsang *et al*., 2005; Kruschwitz and Yaramanci, 2004; Kim *et al*., 2011; Lee *et al*., 2013). Fracture properties in the EDZ are quite dynamic and evolve over time as hydromechanical conditions change. Understanding and modeling the coupled processes and their impact on repository performance are critical for any defensible performance assessment of a radioactive waste repository in clay/shale host rock.

Modeling of the formation and evolution of EDZ is very challenging. In recent years, extensive work on the EDZ modelling has been performed by the researchers all over the world and several Workshops on EDZ were held. There is a large body of research literature available on the EDZ (Martino and Martin, 1996; Martino, 2003; Davies and Bernier, 2005; Tsang *et al*., 2005; Lee *et al*., 2013). Based on the previous studies, it is generally accepted that it is important to ensure the numerical model is capable of characterizing the entire fracturing process involving the initiation, propagation, and coalescence of micro-cracks in the host rock, and that modeling results indeed represent the physics of the involved processes (Tsang *et al*., 2012; Kim *et al*., 2011; Lee *et al*., 2013). For numerous cases, the progressive failure mechanisms of local damage lead to a global failure of tunnel. This progressive failure explains the physical mechanism between the initial localized surface spalling and the entire EDZ formation (Martino, 2003; Kim *et al*., 2011; Li *et al*., 2013; Lin *et al*., 2013; 2014).

In addition to the typical challenges of EDZ analysis in rock, modeling of the EDZ extent depends on the constitutive law used and there has been further concern regarding the short-term stress-strain behavior of rock, because analysis using linear-elastic or elasto-plastic methods based on conventional Hooke's law has, as previously indicated, generally been unsatisfactory in capturing the nonlinear deformation behavior of a rock mass. It has been widely reported that in many cases, during the

*Associate Professor, School of Civil Engineering, Dalian University of Technology, Dalian 116024, China (Corresponding Author, E-mail: li_lianchong@yahoo.com)

**Career Staff Scientist, Earth Science Division, Lawrence Berkeley National Laboratory, Berkeley CA94720, United States (E-mail: hhliu@lbl.gov)

excavation of underground tunnel openings, unusually large deformations have been observed around these openings (Nawrocki *et al*., 1998; Lionco and Assis, 2000; Corkum and Martin, 2007; Weng *et al*., 2008; Tsang *et al*., 2012).

To further improve the understanding and modeling the EDZ in clay/shale host rock, in this study, a recently proposed stress-strain relationship, called the two-part Hooke's model (TPHM), is introduced and implemented in a geomechanical simulator. Then, using field measured data from ED-B tunnel at Mont Terri URL (Bossart and Thury, 2008), the model is calibrated and validated for its ability to predict the nonlinear deformation and EDZ behaviour of clay rock to excavation. The incorporation of the TPHM in the analysis is expected to more accurately capture the deformation, failure mode, and associated hydromechanical behavior of the rock mass around ED-B tunnel.

2. Two-Part Hooke's Model (TPHM) and Its Implementation in the Three-Dimensional Finite Difference Program, FLAC3D

2.1 A Brief Introduction to the Two-Part Hooke's Model (TPHM)

The stress-strain relationship is the most fundamental part of constitutive relationships. Hooke's law has been generally used to describe this stress-strain relationship for elastic mechanical processes. According to Hooke's law, for elastic material, the proportionality in the stress-strain relationship should be constant. However, this proportionality is in fact not always constant in many cases, but rather stress-dependent (e.g., Cazacu, 1999; Lionço and Assis, 2000; Brown *et al*., 1989; Johnson and Rasolofosaon, 1996; Brady, 1969). A number of efforts have been made to relate this stress-dependent behavior to the microstructures of "cracks" in porous rock (Walsh, 1965; Nur, 1971; Mavko and Nur, 1978) – an excellent review of these efforts is provided in a chapter entitled "Micromechanical Models" in Jaeger *et al*. (2007). Because it is generally difficult to characterize small-scale structures accurately and then relate their properties to large-scale mechanical properties that are of practical interest, it is desirable to have a macroscopic-scale theory that does not rely on the detailed description of small-scale structures, and that can physically incorporate the stress-dependent behavior of relevant mechanical properties. A theory of this kind was developed within the framework of Hooke's law by Liu *et al*. (2009) and is referred to as "TPHM" in this study.

Liu *et al*. (2009) argued that different varieties of Hooke's law should be applied within regions of the rock having significantly different stress-strain behavior, and that a rock body could be conceptualized into two distinct parts. These two parts are called a "hard part," which undergoes only small deformation, and a "soft part," which undergoes large deformation. The natural strain (volume change divided by rock volume at the current stress state), rather than the engineering strain (volume change divided by the unstressed rock volume), should be used in Hooke's law for accurate modeling of the elastic deformation of

the pore volume's soft part, subject to a relatively large degree of relative deformation (i.e., cracks or fractures). This approach permits the derivation of constitutive relationships between stress and a variety of mechanical and/or hydraulic rock properties. The theoretical predictions using this method are generally consistent with empirical expressions and also laboratory rock experimental data (Liu *et al*., 2009; Zhao and Liu, 2012).

2.2 Implementation of TPHM in FLAC3D

In this study, all numerical simulations were conducted using the three-dimensional finite difference program, FLAC3D (Itasca Consulting Group, 2005), a powerful numerical tool that has been widely used in the fields of geotechnical, geomechanical, civil and mining engineering. FLAC3D uses dynamic equations of motion in its explicit, time-marching scheme. The solution of solid body problems in FLAC3D invokes the equations of motion (Newton's law of motion), constitutive relationships, and boundary conditions.

When running the FLAC3D code in its mechanical or thermo-mechanical configuration mode, it solves the equation of motion,

$$\nabla \cdot \mathbf{\sigma} + \rho_m \mathbf{g} = \rho_m \frac{d\mathbf{v}}{dt} \tag{1}$$

in an iterative manner with the $\mathbf{\sigma}$ stress-strain relationship, where ρ_m is average density of the rock mass and $\mathbf{v}$ is solid velocity with respect to a fixed system. The incremental stress and strain during a time step is governed by various elastic or elasto-plastic constitutive laws, which can be written in a general form as:

$$\Delta\sigma' = \mathbf{H}(\sigma', \varepsilon\Delta t) \tag{2}$$

in which $\mathbf{H}$ contains given material functions, $\dot{\varepsilon}$ is the infinitesimal strain-rate tensor, and Δt is a time increment. The constitutive laws in Eq. (2) work on the effective stress, which can be calculated as:

$$\mathbf{\sigma'} = \mathbf{\sigma} + \mathbf{I}\alpha P \tag{3}$$

where α is Biot's effective stress parameter (Biot, 1941) and P is pore pressure.

FLAC3D provides material models such as Mohr-Coulomb and Hoek-Brown failure criteria that are suitable for geotechnical materials. All of these models are provided as Dynamic-Linked Libraries (DLLs) that are loaded when FLAC3D is first executed. Users can modify these models or create their own constitutive models as DLLs.

All constitutive models in FLAC3D share the same incremental numerical algorithm. Given the stress state at time t, and the strain increment for a time step Δt, the purpose of the constitutive models is to determine the corresponding stress increment and the new stress state at time $t+\Delta t$. When plastic deformations are involved, only the elastic part of the strain increment will contribute to the stress increment. In this case, a correction must be made to the elastic stress increment (as computed from the total strain increment) in order to obtain the actual stress state for the new time step.

As a stress-strain relationship, the TPHM can be implemented into any models provided by FLAC3D. There are thirteen basic

constitutive models provided in FLAC3D, arranged into null, elastic, and plastic model groups. The most commonly used criteria plastic-model groups are those of Mohr-Coulomb, Hoek and Brown, the Cam-Clay model, in which the Mohr-Coulomb model is often used to represent failure in soils and rocks because of its simple form (Vermeer and deBorst, 1984; Sheldon, 2009; Itasca Consulting Group, 2005). In this study, TPHM was implemented into the Mohr-Coulomb model.

In FLAC3D, the failure envelope for the Mohr-Coulomb model corresponds to a Mohr-Coulomb criterion (shear yield function) with tension cutoff (tension yield function). Note that all models in FLAC3D operate on effective stresses only. The Mohr-Coulomb criterion in FLAC3D is expressed in terms of the principal stresses σ_1, σ_2, and σ_3, which are the three components of the generalized stress vector for this model. Mohr-Coulomb failure criterion is expressed as:

$$f^S = \sigma_1 - \sigma_3 N_\varphi + 2c\sqrt{N_\varphi} \qquad (4)$$

and the tension failure criterion is expressed as:

$$f^t = \sigma_3 - \sigma^t \qquad (5)$$

where φ is the friction angle, c is the cohesion, σ^t is the tensile strength, and $N_\varphi = (1 + \sin\varphi)/(1 - \sin\varphi)$.

In the implementation of the Mohr-Coulomb model in FLAC3D, a trial stress (σ_{ij}) is first computed by application of Hooke's law to the strain increments $\Delta\varepsilon_{ij}$. In the elastic, isotropic model, strain increments generate stress increments according to the conventional Hooke's law (Single-part Hooke's model, abbreviated as SPHM):

$$\Delta\sigma_{ij}^{SPHM} = 2G\Delta\varepsilon_{ij} + \alpha_2 \Delta\varepsilon_{kk}\delta_{ij} \qquad (6)$$

where the Einstein summation convention applies, δ_{ij} is the Kroenecker delta symbol $\delta_{ij} = \begin{cases} 1,(i=j) \\ 0,(i\neq j) \end{cases}$, and α_2 is a material constant related to the bulk modulus, K, and shear modulus, G, as $\alpha_2 = K - (2/3)G$.

New stress values, elastic guess (σ_{ij}^I), are then obtained from the relationship

$$\sigma_{ij}^I = \sigma_{ij}^O + \Delta\sigma_{ij}^{SPHM} \qquad (7)$$

where σ^O are the initial stresses at time t. The principal stresses σ_1^I, σ_2^I, σ_3^I and corresponding directions are then calculated. If the stresses σ_1^I, σ_2^I, σ_3^I violate the composite yield criterions, Eqs. (4) or (5), plastic deformation takes place. The new principal stress components are corrected by using the plastic flow rule to ensure that they lie on the yield surface. If point (σ_1^I, σ_3^I) is located below the representation of the composite failure envelope in the plane (σ_1, σ_1), no plastic flow takes place for this step, and the new principal stresses are given by σ_i^I, (i = 1,3).

In an anisotropic stress condition, TPHM is given by:

$$\varepsilon_1 = \frac{(3-\gamma_t)}{3E_e}[\sigma_1 - \nu(\sigma_2 + \sigma_3)] + \frac{\gamma_t}{3}\left[1 - \exp\left(-\frac{\sigma_1}{E_t}\right)\right]$$
$$\varepsilon_2 = \frac{(3-\gamma_t)}{3E_e}[\sigma_2 - \nu(\sigma_1 + \sigma_3)] + \frac{\gamma_t}{3}\left[1 - \exp\left(-\frac{\sigma_2}{E_t}\right)\right] \qquad (8)$$
$$\varepsilon_3 = \frac{(3-\gamma_t)}{3E_e}[\sigma_3 - \nu(\sigma_2 + \sigma_1)] + \frac{\gamma_t}{3}\left[1 - \exp\left(-\frac{\sigma_3}{E_t}\right)\right]$$

where σ_1, σ_2, σ_3 are effective principal stresses, ε_1, ε_2, ε_3 are principal engineering strains (stresses and strains are assumed to have the same principal orientation), ν is Poisson ratio for the hard part, γ_t is the ratio of the soft part to the entire rock body in one principal orientation and has a value, obtained through experimental tests, on order $10^{-1} \sim 10^{-2}$, and E_e and E_t refer to Young's (elastic) modulus for the hard and soft part, respectively (Zhao and Liu, 2012). Note that for $\gamma_t = 0$, Eq. (8) is reduced to the conventional stress-strain relationship (the conventional Hooke's law, SPHM).

To implement the numerical routine in FLAC3D, we transform the principal stress/strain coordinate system into a global coordinate system (x, y, z). Based on Eq. (8), the general stress-strain relationship in a global coordinate system (x, y, z) can be calculated as:

$$\begin{aligned}
\varepsilon_x &= \frac{(3-\gamma_t)}{3E_e}[\sigma_x - \nu(\sigma_y + \sigma_z)] + \frac{\gamma_t}{3}\left[1 - \exp\left(-\frac{\sigma_1}{E_t}\right)l_1^2 - \exp\left(-\frac{\sigma_2}{E_t}\right)l_2^2 - \exp\left(-\frac{\sigma_3}{E_t}\right)l_3^2\right] \\
\varepsilon_y &= \frac{(3-\gamma_t)}{3E_e}[\sigma_y - \nu(\sigma_x + \sigma_z)] + \frac{\gamma_t}{3}\left[1 - \exp\left(-\frac{\sigma_1}{E_t}\right)m_1^2 - \exp\left(-\frac{\sigma_2}{E_t}\right)m_2^2 - \exp\left(-\frac{\sigma_3}{E_t}\right)m_3^2\right] \\
\varepsilon_z &= \frac{(3-\gamma_t)}{3E_e}[\sigma_z - \nu(\sigma_x + \sigma_y)] + \frac{\gamma_t}{3}\left[1 - \exp\left(-\frac{\sigma_1}{E_t}\right)n_1^2 - \exp\left(-\frac{\sigma_2}{E_t}\right)n_2^2 - \exp\left(-\frac{\sigma_3}{E_t}\right)n_3^2\right] \\
\gamma_{xy} &= \frac{2(3-\gamma_t)(1+\nu)}{3E_e}\tau_{xy} + \frac{2\gamma_t}{3}\left[\exp\left(-\frac{\sigma_1}{E_t}\right) - \exp\left(-\frac{\sigma_2}{E_t}\right)\right]l_2 m_2 + \frac{2\gamma_t}{3}\left[\exp\left(-\frac{\sigma_1}{E_t}\right) - \exp\left(-\frac{\sigma_3}{E_t}\right)\right]l_3 m_3 \\
\gamma_{xz} &= \frac{2(3-\gamma_t)(1+\nu)}{3E_e}\tau_{xz} + \frac{2\gamma_t}{3}\left[\exp\left(-\frac{\sigma_1}{E_t}\right) - \exp\left(-\frac{\sigma_2}{E_t}\right)\right]l_2 n_2 + \frac{2\gamma_t}{3}\left[\exp\left(-\frac{\sigma_1}{E_t}\right) - \exp\left(-\frac{\sigma_3}{E_t}\right)\right]l_3 n_3 \\
\gamma_{yz} &= \frac{2(3-\gamma_t)(1+\nu)}{3E_e}\tau_{yz} + \frac{2\gamma_t}{3}\left[\exp\left(-\frac{\sigma_1}{E_t}\right) - \exp\left(-\frac{\sigma_2}{E_t}\right)\right]m_2 n_2 + \frac{2\gamma_t}{3}\left[\exp\left(-\frac{\sigma_1}{E_t}\right) - \exp\left(-\frac{\sigma_3}{E_t}\right)\right]m_3 n_3
\end{aligned}$$
$$(9)$$

where x, y, z denote the directions of coordinate axes in a global coordinate system (x, y, z), $l_i = \cos(i, x)$, $m_i = \cos(i, y)$, $n_i = \cos(i, z)$, and $i = 1, 2, 3$ is the index for the direction of the ith principal stress. The functions $\cos(i, x)$, $\cos(i, y)$ and $\cos(i, z)$ are the cosine of the angles between i and the $x, y,$ and z directions, respectively, and are given as:

$$\begin{aligned}
\cos(i, x) &= \frac{(\sigma_y - \sigma_i)(\sigma_z - \sigma_i) - \tau_{zy}\tau_{yz}}{\sqrt{[(\sigma_y - \sigma_i)(\sigma_z - \sigma_i) - \tau_{zy}\tau_{yz}]^2 + [\tau_{zy}\tau_{xz} - \tau_{xy}(\sigma_z - \sigma_i)]^2 + [\tau_{yz}\tau_{yz} - \tau_{xz}(\sigma_y - \sigma_i)]^2}} \\
\cos(i, y) &= \frac{\tau_{zy}\tau_{xz} - \tau_{xy}(\sigma_z - \sigma_i)}{\sqrt{[(\sigma_y - \sigma_i)(\sigma_z - \sigma_i) - \tau_{zy}\tau_{yz}]^2 + [\tau_{zy}\tau_{xz} - \tau_{xy}(\sigma_z - \sigma_i)]^2 + [\tau_{yz}\tau_{yz} - \tau_{xz}(\sigma_y - \sigma_i)]^2}} \\
\cos(i, z) &= \frac{\tau_{xy}\tau_{yz} - \tau_{xz}(\sigma_y - \sigma_i)}{\sqrt{[(\sigma_y - \sigma_i)(\sigma_z - \sigma_i) - \tau_{zy}\tau_{yz}]^2 + [\tau_{zy}\tau_{xz} - \tau_{xy}(\sigma_z - \sigma_i)]^2 + [\tau_{yz}\tau_{yz} - \tau_{xz}(\sigma_y - \sigma_i)]^2}}
\end{aligned}$$
$$(10)$$

To incorporate the TPHM into the Mohr-Coulomb model within FLAC3D, the stress increments, $\Delta\sigma_{ij}^{SPHM}$, in Eq. (7) is replaced by $\Delta\sigma_{ij}^{TPHM}$. The $\Delta\sigma_{ij}^{TPHM}$ can be directly obtained by calculating the following equation:

$$\begin{aligned}
d\varepsilon_x &= \frac{(3-\gamma_t)}{3E_e}[d\sigma_x - \nu(d\sigma_y + d\sigma_z)] + d\varepsilon_{xt} \\
d\varepsilon_y &= \frac{(3-\gamma_t)}{3E_e}[d\sigma_y - \nu(d\sigma_x + d\sigma_z)] + d\varepsilon_{yt} \\
d\varepsilon_z &= \frac{(3-\gamma_t)}{3E_e}[d\sigma_z - \nu(d\sigma_x + d\sigma_y)] + d\varepsilon_{zt} \\
d\gamma_{xy} &= \frac{2(3-\gamma_t)(1+\nu)}{3E_e}d\tau_{xy} + d\gamma_{xyt} \\
d\gamma_{xz} &= \frac{2(3-\gamma_t)(1+\nu)}{3E_e}d\tau_{xz} + d\gamma_{xzt} \\
d\gamma_{yz} &= \frac{2(3-\gamma_t)(1+\nu)}{3E_e}d\tau_{yz} + d\gamma_{yzt}
\end{aligned} \qquad (11)$$

Equation (11) is an incremental formulation of Eq. (9). In Eq. (11,) the strain increments $d\varepsilon_x$, $d\varepsilon_y$, $d\varepsilon_z$, $d\gamma_{xy}$, $d\gamma_{xz}$, $d\gamma_{yz}$ are known values, i.e., $\Delta\varepsilon_{ij}$; while the last items $d\varepsilon_{xt}$, $d\varepsilon_{yt}$, $d\varepsilon_{zt}$, $d\gamma_{xyt}$, $d\gamma_{xzt}$, $d\gamma_{yzt}$ are the strain increments for the soft part and can be expressed as:

$$de_{xt} = \frac{\gamma_t}{3E_t}\left[\exp\left(-\frac{\sigma_1}{E_t}\right)l_1^2 d\sigma_1 + \exp\left(-\frac{\sigma_2}{E_t}\right)l_2^2 d\sigma_2 + \exp\left(-\frac{\sigma_3}{E_t}\right)l_3^2 d\sigma_3\right]$$

$$de_{yt} = \frac{\gamma_t}{3E_t}\left[\exp\left(-\frac{\sigma_1}{E_t}\right)m_1^2 d\sigma_1 + \exp\left(-\frac{\sigma_2}{E_t}\right)m_2^2 d\sigma_2 + \exp\left(-\frac{\sigma_3}{E_t}\right)m_3^2 d\sigma_3\right]$$

$$de_{zt} = \frac{\gamma_t}{3}\left[\exp\left(-\frac{\sigma_1}{E_t}\right)n_1^2 d\sigma_1 + \exp\left(-\frac{\sigma_2}{E_t}\right)n_2^2 d\sigma_2 + \exp\left(-\frac{\sigma_3}{E_t}\right)n_3^2 d\sigma_3\right]$$

$$d\gamma_{xyt} = \frac{2\gamma_t}{3E_t}\left[\exp\left(-\frac{\sigma_2}{E_t}\right)d\sigma_2 - \exp\left(-\frac{\sigma_1}{E_t}\right)d\sigma_1\right]l_2 m_2 + \frac{2\gamma_t}{3}\left[\exp\left(-\frac{\sigma_3}{E_t}\right)d\sigma_3 - \exp\left(-\frac{\sigma_1}{E_t}\right)d\sigma_1\right]l_3 m_3$$

$$d\gamma_{xzt} = \frac{2\gamma_t}{3E_t}\left[\exp\left(-\frac{\sigma_2}{E_t}\right)d\sigma_2 - \exp\left(-\frac{\sigma_1}{E_t}\right)d\sigma_1\right]l_2 n_2 + \frac{2\gamma_t}{3}\left[\exp\left(-\frac{\sigma_3}{E_t}\right)d\sigma_3 - \exp\left(-\frac{\sigma_1}{E_t}\right)d\sigma_1\right]l_3 n_3$$

$$d\gamma_{yzt} = \frac{2\gamma_t}{3E_t}\left[\exp\left(-\frac{\sigma_2}{E_t}\right)d\sigma_2 - \exp\left(-\frac{\sigma_1}{E_t}\right)d\sigma_1\right]m_2 n_2 + \frac{2\gamma_t}{3}\left[\exp\left(-\frac{\sigma_3}{E_t}\right)d\sigma_3 - \exp\left(-\frac{\sigma_1}{E_t}\right)d\sigma_1\right]m_3 n_3$$

$$\tag{12}$$

In Eq. (12), the principal stresses σ_1, σ_2, and σ_3 are the known values. Based on the stress transformations in three dimensions (Poulos and Davis, 1974; Jaeger *et al*., 2007), one can obtain σ_1, σ_2, and σ_3 using the stresses σ_{ij}^O at time t. An algorithm function for calculating σ_1, σ_2, and σ_3 has been provided by the module of the C++ source code for the Mohr-Coulomb model in FLAC3D. While the principal stress increments $d\sigma_1$, $d\sigma_2$, and $d\sigma_3$ in Eq. (12) can be expressed as:

$$d\sigma_1 = d\sigma_x l_1^2 + d\sigma_y m_1^2 + d\sigma_z n_1^2 + 2d\tau_{xy}l_1 m_1 + 2d\tau_{xz}l_1 n_1 + 2d\tau_{yz}m_1 n_1$$

$$d\sigma_2 = d\sigma_x l_2^2 + d\sigma_y m_2^2 + d\sigma_z n_2^2 + 2d\tau_{xy}l_2 m_2 + 2d\tau_{xz}l_2 n_2 + 2d\tau_{yz}m_2 n_2$$

$$d\sigma_3 = d\sigma_x l_3^2 + d\sigma_y m_3^2 + d\sigma_z n_3^2 + 2d\tau_{xy}l_3 m_3 + 2d\tau_{xz}l_3 n_3 + 2d\tau_{yz}m_3 n_3$$

$$\tag{13}$$

where l_i, m_i, and n_i ($i=1, 2, 3$) can be calculated by Eq. (10). Based on Eqs 11, 12 and 13, we can get $d\sigma_x$, $d\sigma_y$, $d\sigma_z$, $d\tau_{xy}$, $d\tau_{xz}$, and $d\tau_{yz}$, that correspond to $\Delta\sigma_{ij}^{TPHM}$ in Eq. (7).

Here, we need to indicate that TPHM is only applicable to compression conditions. Under a tension condition, the strain for the soft part would become unrealistically large because of the exponential dependence of strain on stress. However, it is reasonable to consider that the soft part, just like a fracture, cannot sustain tensions, and thus SPHM is used in this case. In other words, if one of the principal stresses is in tension, the strain for the soft part in the same direction as principal stress will be omitted. Then SPHM is used in this principal orientation (Eq. (6)), and TPHM is used in the other principal orientations. If all of the three principal stresses are in tension, the stress increments are still given by Eq. (6). The computational scheme implemented FLAC3D is shown in Fig. 1. The modified Mohr-Coulomb model written in C++ was compiled as a DLL file that can be loaded whenever it is needed.

Rock consists of crystals, grains, voids, pores, cracks, and the like. As a consequence, in order to trace isolated fracture processes, heterogeneity must be represented and introduced appropriately (Fang and Harrison, 2002; Wong *et al*., 2006; Ma *et al*., 2011). In this study, the new constitutive relationship is incorporated at element (zone) level. The mechanical parameters of the element, such as Young's modulus, strength, and Poisson's ratio, are
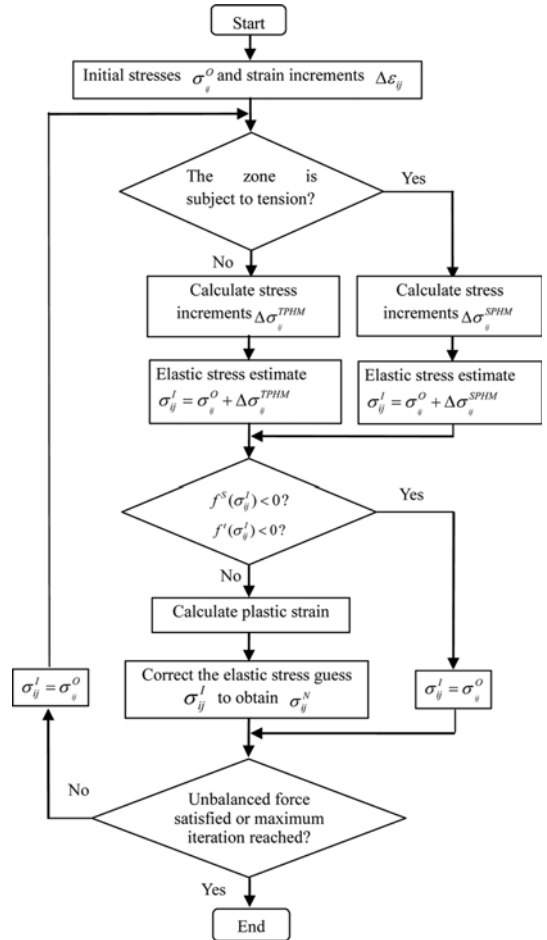

Fig. 1. Computational Scheme for the Numerical Implementation of the TPHM into FLAC3D

heterogeneous and assumed to conform to the Weibull distribution (Weibull, 1951):

$$f(u) = \frac{m}{u_0}\left(\frac{u}{u_0}\right)^{m-1}\exp\left(-\frac{u}{u_0}\right)^m \tag{14}$$

where u is the parameter of the element (such as the Young's modulus, Poisson's ratio, strength properties, permeability, and heat conductivity), the scale parameter u_0 is related to the average of the element parameter, and the homogeneity index m defines the shape of the distribution function and represents the degree of material homogeneity. A heterogeneous material can be produced numerically in a computer simulation for a material composed of many elements. Each element is assumed to be isotropic and homogeneous. Higher homogeneity indices lead to more homogeneous numerical samples (Tang *et al*., 2000; Wong *et al*., 2006).

It is generally known that the progressive degradation of material properties results from the initiation, growth, and coalescence of microcracks, which eventually induce the macroscopic failure. In terms of degradation, it is seen from stress-strain curves that, in uniaxial compression, the rock displays sudden degradation in both strength and stiffness (i.e., very brittle behavior) after attain-

ment of the peak stress. The mechanical behavior of rock evolves from elastic-brittle to elastic-brittle-ductile with increasing confining pressure. Using this observation in conjunction with idealized piece-wise linear differential stress-strain curves, studies have been shown that degradation in both strength and stiffness can be unified through a degradation index r_d (Fang and Harrison, 2002), which may be formulated as:

$$r_d = \frac{\delta\sigma_p}{\delta\sigma_0} = \frac{\delta S_p}{\delta S_0} \tag{15}$$

As shown in the diagram of Fig. 2, σ_c and σ_{cd} are the peak strength and residual strength under uniaxial stress state, and σ_p and σ_{pd} are the hypothetical peak strength and residual strength with confining pressure. The terms $\delta\sigma_0$ and $\delta\sigma_p$ are the strength differences for the uniaxial and general triaxial conditions, respectively. Terms $\delta S_0(=S_0 - S_{0d})$ and $\delta S_p(=S_0 - S_{pd})$ are the corresponding stiffness differences. The definition of the degradation index implies that the value of r_d ranges from zero (no degradation, ductile failure) to unity (complete degradation, brittle failure). It has been suggested (Fang and Harrison, 2002) that the relationship between the degradation index and confining pressure can conveniently be expressed as:

$$r_d = \exp(-n_d\sigma_3) \tag{16}$$

where n_d is a degradation parameter and σ_3 is the confining pressure. This index has been shown to be capable of describing the degrading behavior of rock under laboratory tests, as well as serving as a functional relationship for modeling the process of rock fracturing.

The degradation of strength and stiffness is an essential component of the local degradation approach. This degradation means that intact rock alters into a more deformable and weaker material. This altered material can conceptually be regarded as being fractured, with the result that other material properties should take on values that are appropriate for a fractured material. Once an element (zone) becomes the conceptual fracture, the residual elemental stiffness, S_r, and the normalized residual strength, σ_r, are thus given by:

$$\left.\begin{array}{l} S_r = S_p(1-r_d) \\ \sigma_r = \sigma_p(1-r_d) \end{array}\right\} \tag{17}$$
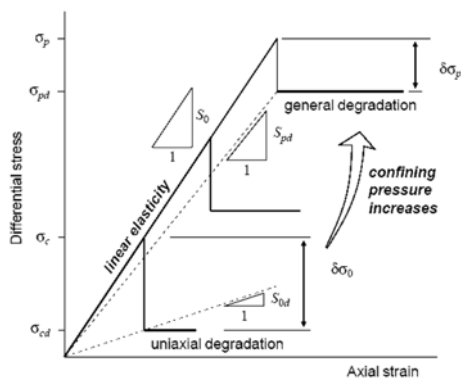

Fig. 2. Sketch of the Definition of the Degradation Indices (Yuan and Harrison, 2005)

On the basis of the above equations that quantify the post-peak degradation, a material suffers from elasticity (no degradation, r_d=0) to complete damage (complete degradation, r_d=1).

In modeling studies with FLAC3D, elements whose ultimate tensile or shear strength has been attained are displayed as cracks with grey or black color in post-processing figures. One of the main features of this type of model is that there is no need for a pre-existing crack to simulate the crack initiation and propagation. This approach to simulating cracks is similar to a smeared crack model, i.e., no special singular element is used − which has the advantage of leaving the mesh topology untouched. Brittle fractures yielded from the initiation and propagation of cracks in arbitrary and complex paths could be properly simulated without additional processes. Microstructure and defects can be represented by different sets of zones with their own material properties. Hence, it is efficient to simulate the heterogeneous materials. A similar principle has been addressed and applied to modeling concrete damage (Pietruszczak and Xu, 1995; Pearce *et al.*, 2000). With the recent advances in computer performance, an increasing number of researchers have attempted to use a similar principle to solve discontinuous problems through continuum mechanics (Fang and Harrison, 2002; Zhu and Tang, 2004; Ma *et al.*, 2011; Pan *et al.*, 2009; 2012).

When an element of rock undergoes dilatancy due to the degradation of strength and stiffness, its hydraulic properties will change. Experimental results indicate that dilatancy leads to an increase in permeability. These changes in hydraulic properties can be directly related to either stress or strain (Louis 1974; Stormont and Daemen, 1992; Zhu and Wong, 1997; Otto Schulze *et al.*, 2001; Tang *et al.*, 2002). Most of the theories regarding stress-induced variations in permeability correspond to the pre-failure phase. During elastic deformation, rock permeability decreases when the rock is compacted and increases when the rock is extended. In order to develop a relation between elastic contraction and permeability, we first employ Eq. (18) to represent the variation in porosity in response to stress.

$$\phi = \phi_0 - \gamma_t - (\phi_0 - \gamma_t)C_e(\sigma_1 + \sigma_2 + \sigma_3)$$
$$+ \frac{\gamma_t}{3}\left[\exp\left(-\frac{\sigma_1}{E_t}\right) + \exp\left(-\frac{\sigma_2}{E_t}\right) + \exp\left(-\frac{\sigma_3}{E_t}\right)\right] \tag{18}$$

where ϕ_0 is the porosity under unstressed conditions, and C_e is the compressibility for the hard fraction of pore volume. The above relationship was derived based on Eq. (8). This new relationship is satisfactorily supported by various types of experimental data for rock from different sources (Liu *et al.*, 2009).

Based on the analysis of a great number of experimental clay-rock data, Yang and Aplin (2010) pointed out that much of the permeability range observed at a given porosity could be explained by variation in lithology. Using clay content as the quantitative lithology descriptor, they proposed that permeability is a function of porosity and clay content:

$$K = \exp(-69.59 - 26.79F_c + 44.07F_c^{0.5} + (-53.61 - 80.03F_c + 132.78F_c^{0.5})$$
$$\cdot \psi + (86.61 + 81.91F_c - 163.61F_c^{0.5}) \cdot \psi^{0.5}) \tag{19}$$

where, F_c is the clay content, $\psi = \phi/(1 - \phi)$. In this study, Eq. (19) is employed to represent the permeability variation in the rock matrix under an elastic state.

In the post-peak stage, rock elements undergo both instantaneous strength degradation and volumetric expansion. Although many experiments have shown that there is a clear correlation between volumetric dilatancy and the increase in permeability of brittle rocks at the micro-scale, it is generally difficult to characterize small-scale elements accurately and then relate their properties to macroscopic hydraulic properties that are of practical interest (Shao *et al*., 2005; Jaeger *et al*., 2007). The degradation is physically manifested as the development of fractures, and this is one of the important concepts addressed in this study. To apply appropriate post-peak hydraulic characteristics, we may find the use of a strain-based formulation for the permeability variation more suitable (Minkoff *et al*., 2003, Yuan *et al*., 2005; Chen *et al*., 2007). On the basis of deformation-dependent permeability proposed by Yuan *et al*. (2005), we assume that a damaged rock element may be represented hydraulically as a volume of rock containing one fracture. This representation is shown conceptually in Fig. 3. Assuming that the fracture is planar and has parallel sides, the aperture (b) of the fractures is given approximately by:

$$b \approx \frac{\Delta V}{l^2} \approx \frac{\varepsilon_v V}{\sqrt[3]{V^2}} = \varepsilon_v \sqrt[3]{V} \tag{20}$$

where ε_v is the volume strain, V is the volume change of the element due to dilatation, and l is the side length of the element before dilatation.

Once the fracture initiated, its aperture will vary with the stress state. Fracture permeability is largely determined by fracture aperture. A number of empirical expressions exist in the literature for describing observed relationships between normal stress and fracture closure (that are linearly related to the average fracture aperture) (Goodman, 1976; Barton *et al*., 1985). In this subsection, we employ such a relationship to represent variations in fracture aperture. Considering a fracture to be embedded into a rock sample subject to normal stress σ_n, we again divide fracture space into "hard" and "soft" parts along the direction normal to the fracture plane. Then, the volumetrically averaged fracture aperture (b) is given by:

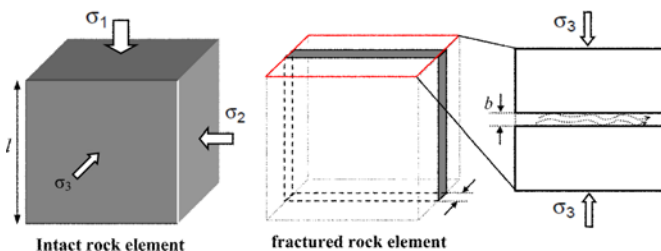$$b = b_{0,e} + b_{0,t}\exp\left(-\frac{\sigma_n}{K_{F,t}}\right) \tag{21}$$

Fig. 3. Schematic Illustration of Fracture Aperture and Permeability of a Rock Element due to Failure

where, $b_{0,e}$ is the fracture aperture of the "hard" part (the value is determined by Eq. (20)), $b_{0,t}$ is the fracture aperture of "soft" part, and $K_{F,t}$ is the stiffness of the "soft" part in the fracture. Eq. (21) was derived from the TPHM. The "soft" part corresponds to a range of apertures whose relative changes with stress are significant for low normal stress (or small contacting areas) and the "hard" part corresponds to the range of apertures associated with stabilized contact areas as stress changes. The stress-dependent behavior of the fracture aperture is controlled by the second term at low stress. The expression has been used successfully to match laboratory measurements (Liu *et al*., 2011; 2013; Wei *et al*., 2013).

The so-called cubic law gives the flow rate between smooth parallel plates as:

$$q = \frac{b^3 \rho_l g}{12\mu_l}\frac{\Delta H}{l} \tag{22}$$

where H is the fluid (water) head loss across the two ends. In Eq. (22), the hydraulic conductivity is given by the term $b^2\rho_l g/12\mu_l$. Therefore, incorporating the fracture aperture governed by Eq. (21), the hydraulic conductivity for a damaged rock element can be expressed as:

$$k_d = \frac{b^3 \rho_l g}{12\mu_l} \tag{23}$$

In this study, Eq. (23) is employed to represent the permeability variation for a damaged rock element.

The establishment of an appropriate model to reflect the permeability evolution in fractured rocks is a challenging task. Particularly the permeability change within damage zone may involve very complex mechanisms of normal closure and opening of micro/macro fractures, and shear dilations of fractures in addition to the interactions in the existing fracture network as shown in Jing *et al*. (2013). Here, we need to indicate that only the effect of normal stress on permeability change is incorporated in this study. To facilitate the calculation of permeability variation, the element damage is abstracted to be a planar fracture perpendicular to the minimum principal stress. More studies along this line are needed to more accurately calculate permeability variations for damaged elements.

3. A TPHM-Based Modeling of the EDZ Evolution around the ED-B Tunnel

3.1 A Brief Introduction to the ED-B Tunnel at Mont Terri Site

In many countries, argillaceous formations are being considered as potential host rocks for deep geological disposal of radioactive waste. The Mont Terri rock laboratory started operation in January 1996 as part of the international Mont Terri project. The laboratory is located near the town of St. Ursanne in the Jura Mountains of northwestern Switzerland. The aim of the project is the geological, hydrogeological, geochemical, and geotechnical characterization of clay formations, specifically Opalinus clay. As shown in Fig. 4 (Bossart and Thury, 2008), the Reconnaissance
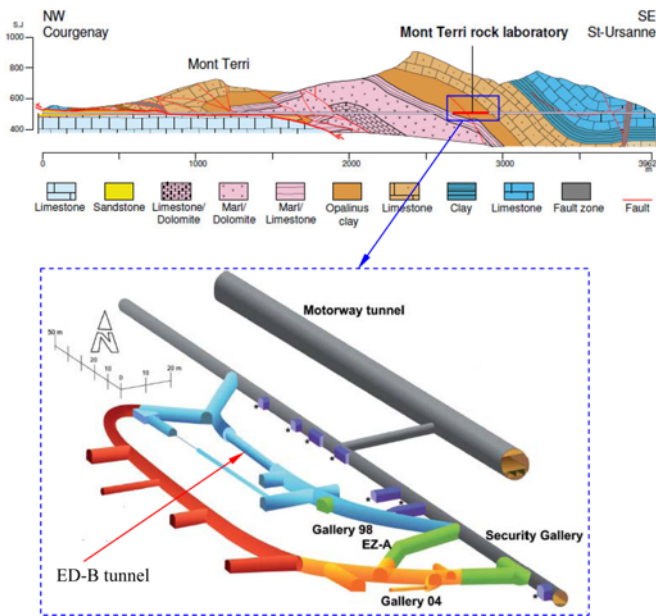
Fig. 4. Vertical Cross Section of the Mont Terri Anticline along the Motorway Tunnel (After Bossart and Thury, 2008)

Gallery (or Security Gallery) was originally constructed as part of the motorway tunnel and the underground laboratory has been developed over the last decade. Where it intersects the laboratory, the Opalinus Clay is about 250 m thick along the length of the tunnel. As a result of differing sedimentation, the Opalinus Clay can be grouped into three facies: sandy facies, carbonate-rich sandy facies and shaly facies, the latter being of most interest for repository construction.

In 1997-1998, a Mine-by experiment tunnel, known as the ED-B tunnel (as shown in Figs. 4 and 5), was excavated at the Mont Terri Rock Laboratory to assess the issues associated with tunnel excavation. The ED-B tunnel is located entirely within the shaly facies. No major fault zone runs through the ED-B tunnel. Structurally controlled instability does not generally play a significant role at the laboratory (Bossart and Thury, 2008). The ED-B tunnel consisted of a 35 m long, 3.6 m diameter circular excavation at a depth of ~270 m. The surrounding rock mass of the tunnel was instrumented prior to tunnel driving, allowing for monitoring of the rock-mass response with tunnel advance (Fierz, 1999). The instrumentation records contain unique deformation signatures that provide insight into the mechanical responses of the Opalinus
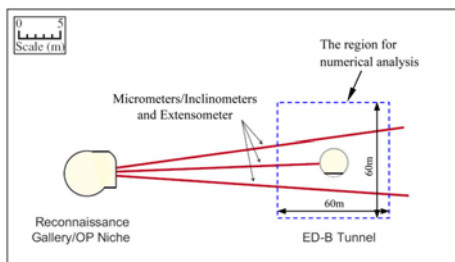
clay to unloading and the formation of an EDZ – a region of micro- and macro-fractured rock mass that forms around the tunnel boundary due to excavation-induced stress redistribution. The resulting data from the experiment can now be used to model the mechanical response to tunnel excavation.

3.2. Numerical Models

To evaluate how accurately the TPHM can reproduce macro-mechanical response of surrounding rock mass around ED-B tunnel, a pseudo 3D numerical model is developed. The geometry and model domain is shown in Fig. 5. The numerical models contain one circular tunnel, consisting of 16,860 zones and 33,978 grid points. The Z-axis is set as vertical in the model, while the horizontal Y- and X-axes are aligned parallel and perpendicular to the tunnel, respectively. The dimensions of the model are 60 m in the X-direction, 1 m in the Y-direction, and 60 m in the Z-direction, respectively. Following the previous studies on tunnels in Opalinus clay (Corkum and Martin, 2007; Bossart *et al.*, 2002; Popp *et al.*, 2008), the mechanical boundary conditions employed in our study include a total stress of σ_x=2.2 MPa, σ_y=4.3 MPa, and σ_z=6.5 MPa, at the outer boundaries. The underground water table is assumed to be located 100 m above the top boundary of the model, and the rock matrix is assumed to be fully saturated. A pore-pressure distribution of P_w=1000000+ $(60 - Z)\rho_w g$ Pa (where Z is height) is directly incorporated into the numerical model. The outer boundary condition is the imposed pressure distribution without change over time. A constant pressure boundary is imposed at the tunnel wall, as the tunnel is excavated.

3.3 Calibration of the Mechanical Parameter Values

Bock (2001) has observed that the stress-strain curves of unconfined compression tests on samples of Opalinus clay have unusually nonlinear stiffness in the low stress region. This behavior is illustrated by the unconfined compression test stress-strain curve for a sample of Opalinus clay, shown in Fig. 6. It can be seen that the deformation behavior of Opalinus clay at low stress levels is characterized by a shallow sloping stress-strain curve near the origin ($0<\sigma<2$ MPa).

To capture the highly nonlinear, low stiffness stress-strain response of Opalinus clay at low stress levels, we employed the newly developed constitutive model, TPHM, to conduct numerical
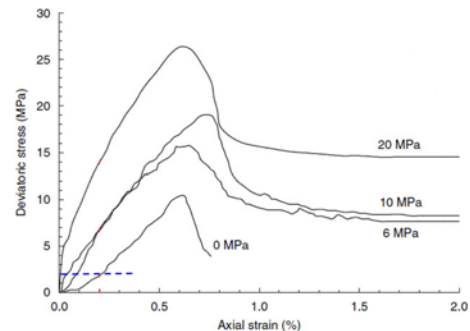

Fig. 5. Layout of ED-B Mine-by Experiment Instrumentation and Tunnel System (Corkum and Martin, 2007)

Fig. 6. Stress-Strain Plots of the Opalinus Clay for a Range of σ_3 Values (0-20 MPa) (Olalla *et al.*, 1999)

simulation in this study. First, we set up a 2D numerical specimen with a width of 80 mm and height of 160 mm, composed of 40×80 elements that are produced randomly by a computer, according to the Weibull distribution for a given homogeneity index. The homogeneity index, m, is a key parameter in this modeling. The analysis and microstructural observations conducted by Wong *et al.* (2006) indicate that values for the Weibull parameter m are greater than 2.0, but fall in the typical range of m =2.0~6.0 (McClintock and Argon, 1966; Liu *et al.*, 2004). We selected the Weibull parameter m=3.0 to describe the heterogeneous material properties of rock in this study. Each elemental zone has individual strength properties, bulk modulus, shear modulus, Poisson's ratio, and dilation angle. During the simulation, the bulk and shear moduli of an elemental zone may degrade once the strength criterion is violated, but the other parameters, such as Poisson's ratio and dilation angle, remain constant throughout the entire course of a simulation. Axial loading is performed with incremental axial displacements being applied in a sequence of steps to the outer surface of the specimen. The rock specimen is represented by the modified FLAC Mohr-Coulomb model (a Mohr-Coulomb model based on TPHM).

Experimental results imply that degradation index, n_d, is a mechanical property of the rock, and that different rocks have different values for n_d in Eq. (16). Laboratory testing is required to determine this parameter for a specific rock. Stress-strain plots for consolidated undrained triaxial tests of Opalinus clay samples at confining stresses of 0, 6, 10, and 20 MPa are shown in Fig. 6. Based on laboratory test results and Eqs. (15) and (16), the degradation index, n_d, is plotted in Fig. 7 showing a value of n_d for Opalinus clay of about 0.0752.

The numerically obtained stress-strain curves for the uniaxial case and the case with a confining stress of 10 MPa are shown in Fig. 8(a). The stress-strain curve of Opalinus clay in uniaxial condition, although it is considered to be a relatively weak rock, is similar to that of brittle rock. It can be seen that the deformation behavior of Opalinus clay at low stress levels is characterized by a shallow sloping stress-strain curve near the origin ($0<\sigma<2$ MPa).The non-linearity at low stresses can be the result of the closure of internal voids, flaws or fractures in the sample. However, in the case with a confining stress, the nonlinear part in the stress-strain curve is disappeared. The corresponding simulated
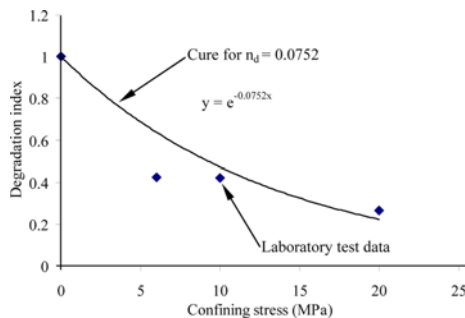
fracture process for uniaxial case is shown in Fig. 8(b), and the numerical results for the case with a confining stress of 10 MPa is shown in Fig. 8(c). Splitting feature is more obvious for the uniaxial case, while shear failure becomes more prominent for the case with a confining stress. Two types of plots are given in the simulation results. One is the cumulative failure pattern, which is a plot of all those elements that have failed during the previous loading history; the other is the active failure pattern, which indicates those elements undergoing degradation within the current time step. In the plots shown here, elements showing historical failure are marked by a grey color, and actively failing elements are marked by a dark color. It is shown that the numerical results based on TPHM are generally consistent with the laboratory results.

Stress-strain data from experimental sources and numerical results show mild to strong non-linear behaviour up to an axial stress of between 1 and 2 MPa. Above this stress threshold, samples are linear elastic with slight nonlinearity after about

(a)

(b1)	(b2)	(b3)	(b4)	(b5)
Random initiation of local failures	Extension and coalescence of failed sites	Further development of site coalescence	Formation of macroscopic fractures	Completion of macroscopic fractures

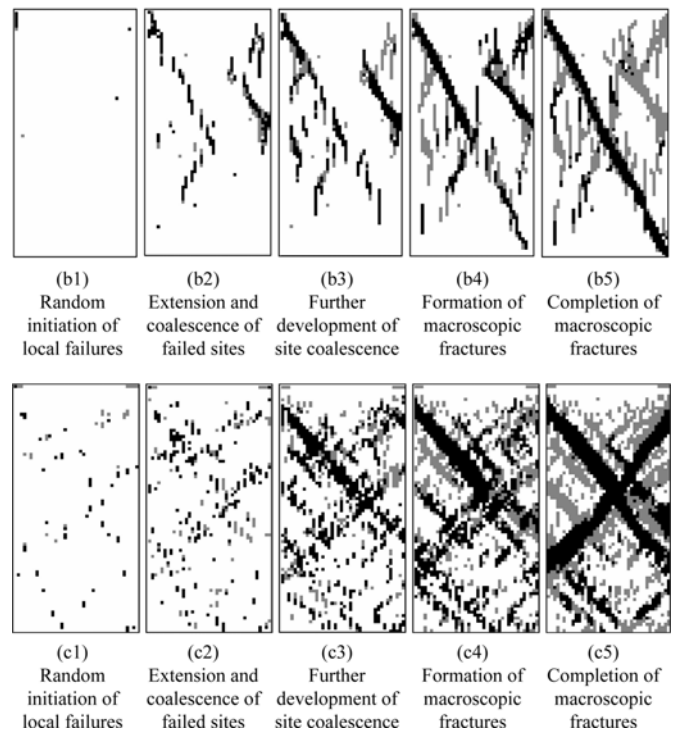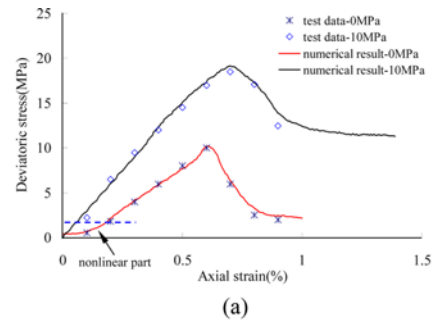| (c1)	(c2)	(c3)	(c4)	(c5)
Random initiation of local failures	Extension and coalescence of failed sites	Further development of site coalescence	Formation of macroscopic fractures	Completion of macroscopic fractures

Fig. 8. Simulated Fracture Process of Opalinus Clay Rock Specimens under Compression: (a) Simulated Stress-Strain Response, (b) The Case under Uniaxial Compression, (c) The Case with a Confining Stress of 10 MPa

Fig. 7. Variation in the Degradation Index for Opalinus Clay with Confining Stress

80% to 90% of peak strength. It is interesting to note that the stress level associated with crack closure corresponds approximately with the minimum in situ stress at Mont Terri ($\sigma_3 \cong 1-3$ MPa (Bossart *et al*., 2004)). The low-stress region is of most interest in the context of unloading around tunnels. Precisely the consequence of unloading process (excavation) is to create a super-low stress region, i.e. the tunnel opening. Once the tunnel opening is formed, the rock mass near the both sidewalls of tunnel opening are almost in uniaxial compression, then the function of the soft part in the TPHM may becomes more prominent and consequently a relatively large deformation in the same direction may be obtained.

Geophysical measurements reported and discussed by Corkum and Martin (2007) indicate an average isotropic Young's modulus for the rock mass of 4 GPa. As a result, an elastic Young's modulus (*E*) of 4 GPa was used for all analyses with elasto-plastic constitutive models. Incorporating a large number of investigations on the properties of Opalinus clay that have been published (Bock *et al*., 2010; Zhang *et al*., 2008; Jobmann *et al*., 2010), the mechanical properties used in the numerical model are summarized in Table 1. The detailed procedure to determine mechanical property values for the soft and hard parts in TPHM, based on observed stress-strain relationships, is given in Liu *et al*. (2009) and Zhao and Liu (2012).

3.4 Numerical Results and Discussion

The deformation around a tunnel induced by excavation was first investigated. The simulated displacement of the rock mass around the tunnel is shown in Fig. 9(a), in which the length of the arrow denotes the magnitude of displacement and the orientation of the arrow denotes the direction of deformation. Obviously, the largest inward displacement occurs at the sidewalls of the tunnel because the sidewalls are subjected to deviatoric stresses capable of inducing extensional fractures, which confirmed by field fracture mapping (Bossar *et al*., 2004). To make a detailed observation on deformation of the rock mass around the tunnel, we select the points located on the micrometer and inclinometers in the model (as shown in Fig. 9b), as the key points for monitoring displacement variations. As a comparison, the response described by conven-
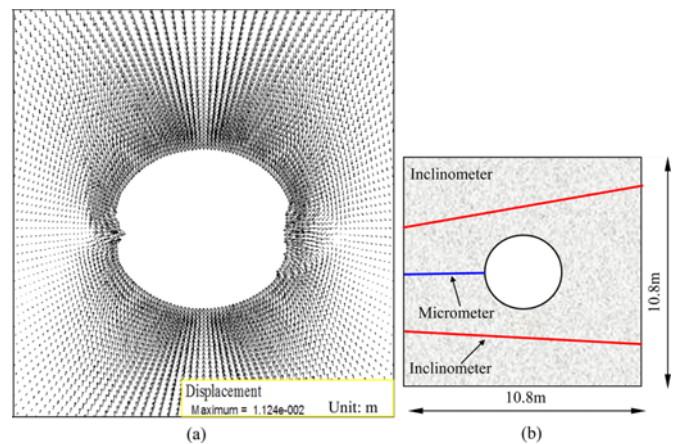

Fig. 9. Deformation Mode of ED-B Tunnel after Excavation and Location of Key Points for Monitoring Displacement Variations Around the Tunnel: (a) The Deformation Mode, (b) The Location of Key Points for Monitoring Displacement Variations around the Tunnel

tional Hooke's law (SPHM) is also numerically obtained with FLAC3D. Fig. 10 is a comparison of deformation distribution based on measured data, TPHM, and SPHM, respectively. It is shown that while the general distribution trend of displacement is similar for both models, the magnitude is clearly different. Numerical results based on TPHM show that the roof and floor of the tunnel recorded a maximum of 7.52 mm of inward movement with the maximum deformation in line with the direction of σ_1. The calculated inward displacements based on the TPHM are larger throughout the tunnel section (including the roof, floor, and sidewalls) compared to those displacements predicted by SPHM. Considering that the displacement was monitored as a function of time and found to increase with time (Corkum and Martin, 2007; Bossart and Thury, 2008; Fierz, 1999), we pay attention only to the observed displacement at the beginning of monitoring. Clearly, the TPHM model results are much closer to the field observations.

Assuming that the pre-peak nonlinearity to be represented by the modulus as a function of the confining stress, the distance from the opening wall, or the combined effects of the hydrostatic, confining, and deviatoric stresses, many studies have captured the stress variation and large deformation around underground openings in rock matrix (Corkuma and Martin, 2007; Lionco and Assis, 2000; Weng *et al*., 2008). Our numerical results are consistent with these previous studies, although the constitutive model employed in this study is different. It can be expected that the incorporation of the TPHM in analyzing the behavior of underground excavations affects not only the displacements and stress distribution, but also the size of the damage zone.

One simple way of estimating the evolution of the EDZ is to use an elastic stress analysis to determine the induced stresses and compare them with the rock-mass strength. The stress is sufficient to create a very thin failed zone in the region of the notch within EDZ, which, however, may significantly underestimate the size of the actual breakout or failed zone. One method, often

Table 1. Physico-Mechanical Parameters Employed in Simulations

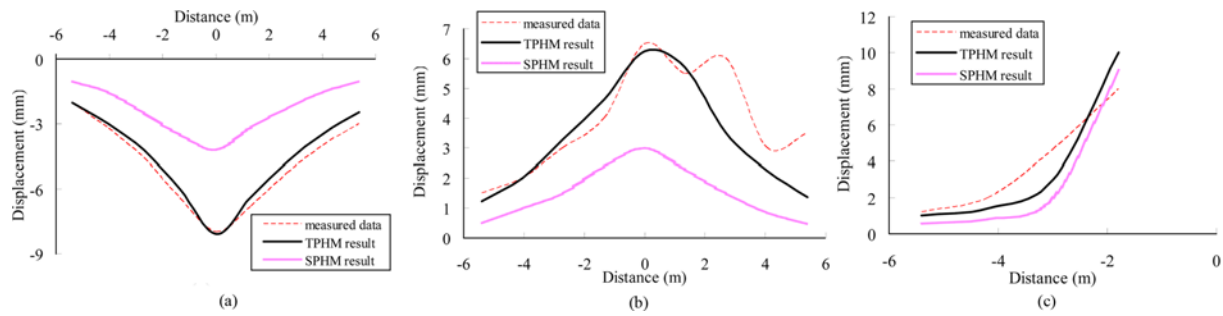| Parameter	Value	Unit
Bulk density (ρ_m)	2450	kg/m^3
Initial porosity (ϕ_0)	0.16	
Young's modulus (E_e)	4	GPa
Poisson's ratio (v)	0.27	
Tensional strength (σ^t)	1.5	MPa
Cohesion (c)	3.6	MPa
Friction angle (φ)	25	°
Clay content (F_c)	60%	
Young's modulus for the soft parts (E_t)	0.002	GPa
γ_t	0.01	
Homogeneity index (m)	3.0	
Degradation index (n_d)	0.0752	

Fig. 10. Displacement Variation at Points the Points Located on the Micrometer and Inclinometers: (a) The Displacement on the Upper Inclinometer, (b) The Displacement on the Bottom Inclinometer, (c) The Displacement on the Micrometer

used to overcome the limitation of elastic analyses, is to simulate the progressive nature of slabbing and spalling in the EDZ formation (Hajiabdolmajid *et al.*, 2002). This method is used in this study, i.e., the EDZ is considered as an interconnected fracture network composed of elements (zones) in plastic state.

In this study, any previously failed neighboring elements (zones) were taken into consideration. After the initial redistribution of stress, some elements may fail due to stress variation. Thus, at each loading step, the stress redistribution procedure is repeated until all of the elements for which the criteria presented in Eq. (4) or (5) are met. The failed elements release stress, and the released stresses are distributed between the intact neighbors, such that global equilibrium of the model is achieved. As the next loading step is achieved, the broken elements form clusters that grow and coalesce with increasing load. Ultimately, the "critical" cluster of the broken elements is formed at a certain loading step. A brittle fracture initiation and propagation is the end result of the micro damage accumulation process, rather than a single event.

The mesh (grid) dependency is unavoidable. Many previous studies focused on aspects related to the mesh effect (Fang and Harrison, 2002; Zhu and Tang, 2004). In general, a finer numerical grid will give higher modeling accuracy, but makes the computation more expensive and time-consuming. In the modeling of EDZ documented in this study, we employed a grid block size of ~0.05 m for the near-field rock mass around the tunnel.

The numerically modeled EDZ evolution around the tunnel is shown in Fig. 11(a). The results indicate that for the given grid system, the damage zone can be fairly well captured by the numerical model, but not individual fractures. The modeled EDZ evolution in this study is the result of quasi-static response of unloading. Initially, tensile damage of scattered elements is observed in the roof and floor, as is the shear damage of scattered elements at the sidewalls. They are individual and do not coalesce with each other to form a crack. Subsequently, more elements in the roof and floor of the opening undergo damage in tensile mode, which eventually leads to the formation of primary (tensile) cracks in the roof and floor. But the cracks in the roof and floor remain stable and do not propagate any further into the surrounding rock mass. In contrast, scattered damaged elements at the sidewalls gradually coalesce with each other to form macroscopic

fractures and continue to propagate into the surrounding rock mass. The shear modes of element damage in the zones of high compression, located at the sidewalls, result in slabbing and crushing. Finally, V-shaped notch zones form at the sidewalls.

The induced damage decreases when moving from the tunnel boundary towards the notch tip. This is in general agreement with the characterization results reported by Hajiabdolmajid *et al.* (2002), which demonstrated that outside the notch, the rock mass was essentially undamaged. The arrest of the observed slabbing process, after a new, more stable, geometry is reached, can be explained by an increase in confinement (progressive frictional strengthening) coupled with a decrease in the induced damage (plastic strain), and thus a decrease in cohesion loss, arresting the failure process and the growth of the notch. Beyond the damaged zone (beyond the notch in the intact rock), where there is no plastic straining, there is no mobilized frictional strength, and the cohesive strength is not affected.

Due to the heterogeneity of the rock, the pattern of fracturing in the rock around the opening is not totally symmetrical. The variation in the fracture mode is highly sensitive to the interaction between the isolated fractures and the local disorder features of the rock matrix within the high-stress field. As a result, the fracturing path is flexural (instead of straight), and the fracture surface is rough. In reality, there are high-stress and low-strength failure types, which occur in different materials. In a homogeneous material, failure begins at a high-stress site, whereas in a heterogeneous material such as rock, failure may start at the weaker locations because of the presence of pores, micro-fractures, grain boundaries, and so on. For this reason, Fairhurst (1964) introduced the notion of "stress severity," which represents the ratio of the theoretical stress at the moment of failure to the stress that would theoretically be necessary for failure to occur at any given point. Heterogeneity is the main reason for the failure that occurs in locations at which the stress is not necessarily the greatest.

The development of fractures is associated with strain softening of the surrounding rock. Localization of micro-cracks and formation of a macroshear plane ("shear band") leads eventually to the full mobilization of the frictional strength after the initial cohesion is lost and reaches its residual value. The process of slabbing around underground openings cannot directly be compared with the shear banding process in laboratory compression tests, even though it also involves a process of cohesion loss and
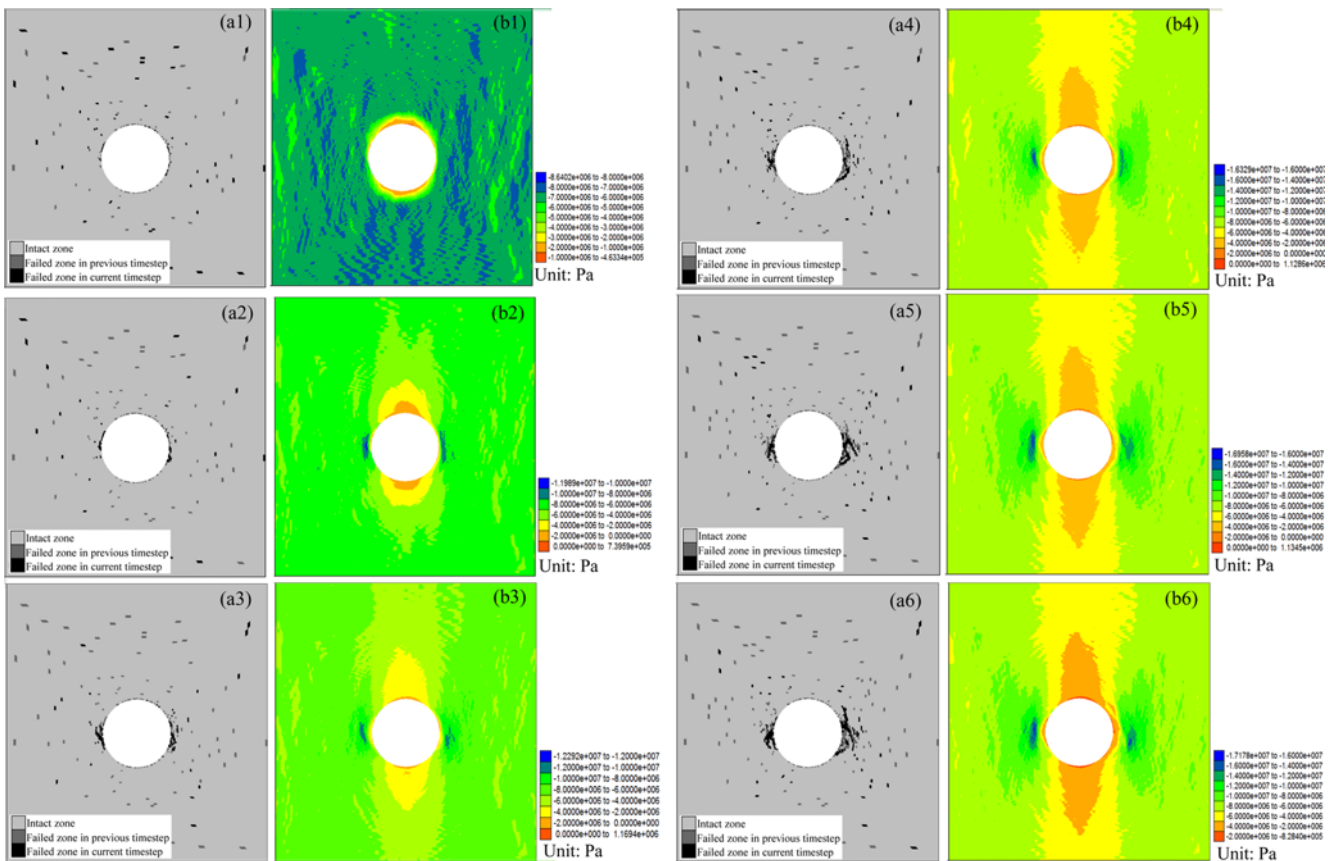
Fig. 11. Numerically Obtained EDZ Evolution: (a) EDZ, (b) Minimum Principal Stress

frictional strength mobilization. Actually, the initially local failure within the "shear band" is tension failure, as shown in Fig. 12. The cohesional component of strength is the predominant strength component at the early stage of brittle failure, with cohesion loss the predominant failure process leading to the observed brittle behavior. The cohesive strength is gradually destroyed by tensile cracking and crack coalescence. The normal stress-dependent frictional strength can only be fully mobilized after the cohesional component of strength is significantly reduced, much damage has accumulated, and rock fragments can move relative to each other in shear. The delay in mobilization of the frictional strength is a characteristic of brittle failure in geomaterials in relatively low-
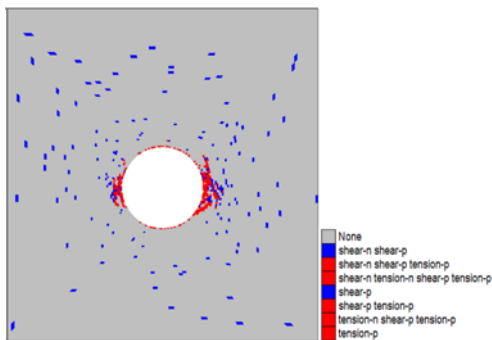
confinement environments, where the brittle fracturing (extensile cracking) is the dominant mode of failure (Tang and Kou, 1998; Hajiabdolmajid *et al*., 2002; Healy *et al*., 2006).

Figure 11(b) shows the stress variation across the opening during EDZ development, which sheds some light on the failure mechanism of the tunnel. Initially, the stress concentrates around the opening adjacent to the tunnel surface. Although the stress distribution at the initial stage is statistically homogeneous on a macroscale, it varies on a microscale due to the microscale heterogeneity in a rock mass. Then, the stress evolution reflects the fracture propagation process. Because of the initiation, propagation, and coalescence of the fracture, a high-stress concentration is induced, and the high-stress concentration zones continuously move forward into surround rock mass. The stress field concentrates around the newly formed fractures, producing further microfracture damage around and ahead of its tips. This continuous stress concentration leads to another new clustering of microfractures. When large fracture zones develop, highly non-uniform stress distributions also develop, especially when the fracture zone is not immediately stress free.

Previous studies show that the hydraulic conductivity values are especially high in the EDZ of the ED-B tunnel, varying between 2.39×10^{-14} m^2 and 7.45×10^{-13} m^2, which means that hydraulic conductivities within the EDZ of ED-B tunnel are orders of magnitude higher when compared to those of undisturbed rock (Bossart *et al*., 2002; Bossart *et al*., 2004). The
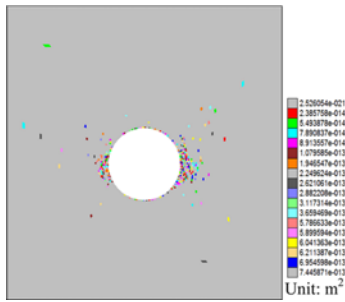

Fig. 12. Failure Type in the EDZ (Tension failure marked by RED color and shear failure marked by BLUE color.)

Fig. 13. Distribution of Hydraulic Conductivity after the Formation of EDZ

Fig. 15. The Final EDZ Mode based on: (a) TPHM and (b) SPHM, Respectively

numerically obtained hydraulic conductivity distribution around the tunnel after EDZ formation is shown in Fig. 13. An interconnected fracture network, connecting to tunnel, with an average extent of 1 m within the tunnel sidewalls is formed. The distribution of hydraulic conductivity generally corresponds with the EDZ mode, in this context, the zone where the hydraulic conductivity is larger than its initial values can be considered as an indicator of the EDZ.

Attempt to predict the maximum depth to which the failure process will propagate is one of the main concerns in the stability of underground opening. Fig. 14 is a conceptual model of EDZ fractures such as steeply inclined unloading joints and shear fractures on both side walls of the ED-B tunnel (Bossart *et al*., 2004). A simple deviatoric stress criterion has been used to estimate the extent of the EDZ fractures in the tunnel walls. An EDZ fracture depth of 0.5~1.0 m in the ED-B tunnel walls was estimated, based on a suggested deviatoric stress value of 8~10 MPa (the value is comparable with the average uniaxial compressive strength of Opalinus clay). Estimated EDZ depth is in good agreement with the inner zone of the EDZ, where an interconnected fracture network is observed in the first meter of the tunnel wall (Bossart *et al*., 2002). In this study, the depth of failure (d_f) was carefully recorded in a progressive, nondestructive manner. To compare the EDZ mode, we also present the results based on SPHM, as shown in Fig. 15. We find that the EDZ extension as calculated by TPHM is relatively larger than that obtained by using the SPHM. The final maximum d_f near sidewalls determined by TPHM is ~1.0 m, while the final maximum d_f is just ~0.5 m for the case based on the SPHM. *In situ* measurement has revealed that the extent of the EDZ is ~1.0 m, but varies between 0.6 and 2.2 m (Schuster *et al*., 2001; Bossart *et al*., 2002; Bossart *et al*., 2004; Martin and Lanyon, 2004).
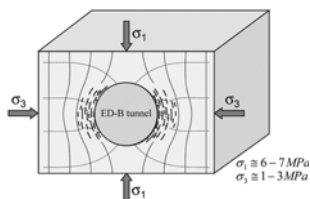

Fig. 14. Conceptual Model of the EDZ and EDZ Fractures in the Tunnel Walls Induced by Stress Redistributions; around ED-B Tunnel after Excavation (Bossart *et al*., 2004)
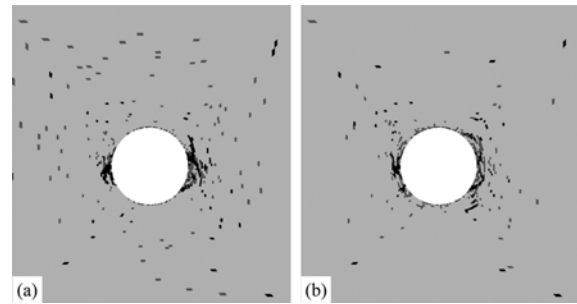
4. Conclusions

Coupled THM processes are critical for EDZ formation and evolution in a clay repository. Understanding and establishing the constitutive relationships involved in these coupled processes are the key elements in modeling these processes. This study has documented an implementation and validation of one recently proposed constitutive relationship (TPHM) and associated numerical results. Based on this study, the following specific conclusions can be made:

1. The TPHM and associated formulations regarding rock hydraulic/mechanical properties were implemented into FLAC3D. This provided the capability for modeling the coupled processes with newly developed constitutive relationships. While TPHM was developed for elastic processes, some features for describing property degradation due to damage and stress-dependence of hydraulic properties of fractures were also considered in the implementation, although this consideration is preliminary at this stage.

2. The usefulness and validity of the TPHM and associated formulations are demonstrated by the consistency between simulation results and field observations from the tunnel excavation at the Mont Terri site. The simulation results, which are sensitive to the constitutive relationships used in the model, capture both the observed displacements and the size of the damage zone, whereas the approach based on the conventional Hooke's law underestimates both. The comparison between simulated and observed results also indicates that laboratory-measured mechanical properties can be used to accurately predict field-scale mechanical deformations, as long as valid constitutive relationships are employed.

3. The EDZ formation and its evolution were numerically modeled, which provides supplementary information on the stress distribution and failure-induced stress redistribution, and shows in detail the propagation of the fracture zone and the interaction of the fractures surrounding the tunnel. The simulations show that the fracturing process in EDZ is caused by the high deviatoric stresses during unloading process (excavation), and that the cohesive strength is gradually destroyed by tensile cracking and crack coalescence. They also indicate that there exist two important mechanisms controlling the permeability variation around the underground opening: (a) the

stress dependency of permeability, which is dominant before the formation of the damage zone around the opening, and (b) the damage-induced permeability increase. The fracture modeling provide insight into the evolution of fractured zone that are impossible to observe in field and are difficult to be considered with static stress analysis approaches.

Acknowledgements

References

Barton, N. R., Bandis, S. C., and Bakhtar, K. (1985). "Strength, deformation, and conductivity coupling of rock joint deformation." *Int. J. Rock Mech. Min. Sci.*, Vol. 22, No. 3, pp. 121-40.

Biot, M. A. (1941). "General theory of three dimensional consolidation." *J. Appl. Phys.*, Vol. 12, No.2, pp.155-164.

Bock, H. (2001). *RA experiment: Rock mechanics analysis and synthesis: Conceptual model of the Opalinus Clay*, Technical Report Nagra, Internal Report TN01-03, Q+S Consult, Germany.

Bock, H., Dehandschutter, B., and Martin, C. D. (2010). *Self-sealing of fractures in argillaceous formations in the context of geological disposal of radioactive waste*, Review and Synthesis. Nuclear Energy Agency, Paris, France.

Bossart, P., Meier, P. M., Moeri, A., Trick, T., and Mayor, J.-C. (2002). "Geological and hydraulic characterization of the excavation disturbed zone in the Opalinus Clay of the Mont Terri Rock Laboratory." *Eng. Geol.*, Vol. 66, Nos. 1-2, pp.19-38.

Bossart, P., Meier, P. M., Moeri, A., Trick, T., and Mayor, J-C. (2004). "Structural and hydrogeological characterisation of the excavation-disturbed zone in the Opalinus Clay (Mont Terri Project, Switzerland)." *Appl. Clay Sci.*, Vol. 26, Nos. 1-4, pp. 429- 448.

Bossart, P. and Thury, M. (2008). *Mont Terri Rock laboratory - Project, programme 1996 to 2007 and results*, Report No. 3 - Swiss Geological Survey, Wabern.

Brady, B. T. (1969). "The nonlinear mechanical behavior of brittle rock Part I — Stress-strain behavior during regions I and II." *Int. J. Rock Mech. Min. Sci.*, Vol. 6, No. 2, pp. 211-225.

Brown, E. T., Bray, J. W., and Santarelli, F. J. (1989). "Influence of stress-dependent elastic moduli on stresses and strains around axisymmetric boreholes." *Rock Mech. Rock Eng.*, Vol. 22, No. 3, pp. 189-203.

Cazacu, O. (1999). "On the choice of stress-dependent elastic moduli for transversely isotropic solids." *Mech. Res. Commun.*, Vol. 26, No. 1, pp. 45-54.

Chen, Y. F., Zhou, C. B., and Sheng, Y. Q. (2007). "Formulation of strain-dependent hydraulic conductivity for a fractured rock mass." *Int. J. Rock Mech. Min. Sci.*, Vol. 44, No. 7, pp. 981-996.

Corkum, A. G. and Martin, C. D. (2007). "Modeling a mine-by test at the Mont Terri rock laboratory, Switzerland." *Int. J. Rock Mech. Min. Sci.*, Vol. 44, No. 6, pp. 846-859.

Davies, C. and Bernier, F. (2005). "Impact of the excavation disturbed or damaged zone (EDZ) on the performance of radioactive waste geological repositories." *Proceedings of the European Commission Cluster Conference and Workshop*, Luxembourg.

Fairhurst, C. (1964). "On the validity of the Brazilian test for brittle materials." *Int. J. Rock Mech. Min. Sci.*, Vol. 1, No. 4, pp. 535-546.

Fang, Z. and Harrison, J. P. (2002). "Development of a local degradation approach to the modelling of brittle fracture in heterogeneous rocks." *Int. J. Rock Mech. Min. Sci.*, Vol. 39, No. 4, pp. 443-457.

Fierz, T. (1999). *ED-B Experiment: Deformation measurements during Phase 4. Inclinometer and sliding micrometer measurements in BED-B6, BED-B7 and BED-B8,* Technical Report Nagra, Internal Report TN99-25, Solexperts, AG.

Goodman, R. E. (1976). *Methods of geological engineering in discontinuous rocks*, West Publishing, New York.

Hajiabdolmajid, V., Kaiser, P. K., and Martin, C. D. (2002). "Modelling brittle failure of rock." *Int. J. Rock Mech. Min. Sci.*, Vol. 39, No. 6, pp. 731-741.

Healy, D., Jones, R. R., and Holdsworth, R. E. (2006). "Three-dimensional brittle shear fracturing by tensile crack interaction." *Nature*, Vol. 439, No. 2, pp. 64-67.

Itasca Consulting Group (2005). *FLAC3D: Fast lagrangian analysis of continuain 3dimensions*, Itasca Consulting Group, Minneapolis.

Jaeger, J. C., Cook, N. G. W. and Zimmerman, R. W. (2007). *Fundamentals of rock mechanics*, 4th Ed., Oxford, Blackwell.

Jing, L., Min, K-B., Baghbanan, A., and Zhao, Z. H. (2013). "Understanding coupled stress, flow and transport processes in fractured rocks." *Geosystem Engineering*, Vol. 16, No. 1, pp. 2-25.

Jobmann, M., Wilsnack, T. H., and Voigt, H. D. (2010). "Investigation of damage-induced permeability of Opalinus clay." *Int. J. Rock Mech. Min. Sci.*, Vol. 47, No. 2, pp. 279-285.

Johnson, P. A., Rasolofosaon, P. N. J. (1996). "Nonlinear elasticity and stressinduced anisotropy in rock." *J. Geophys. Res.*, Vol. 101, No. B2, pp. 3113-3124.

Kim, J., Kwon, S., Sanchez, M., and Cho, G. (2011). "Geological storage of high level nuclear waste." *KSCE Journal of Civil Engineering*, Vol. 15, No. 4, pp. 721-737.

Kruschwitz, S. and Yaramanci, U. (2004). "Detection and characterization of the disturbed rock zone in claystone with the complex resistivity method." *J. Appl. Geophys.*, Vol. 57, No. 1, pp. 63-79.

Lee, C., Lee, D., and Jeon, S. (2013). "The influence of excavation damaged zone on the mechanical and thermal behavior of cement mortar block around an opening." *KSCE Journal of Civil Engineering*, Vol. 17, No. 6, pp. 1263-1274.

Li, L. C., Tang, C. A., Wang, S. Y., and Yu, J. (2013). "A coupled thermo-hydrologic-mechanical damage model and associated application in a stability analysis on a rock pillar." *Tunn. Undergr. Sp. Tech.*, Vol. 34, pp. 38-53.

Lin, P., Zhou, W. Y., and Liu, H. Y. (2014). "Experimental study on cracking, reinforcement and overall stability of the Xiaowan super-high arch dam." *Rock Mech. Rock Eng.*, DOI: 10.1007/s00603-014-0593-x.

Lin, P., Zhou, Y. N., Liu, H. Y., and Wang, C. (2013). "Reinforcement design and stability analysis for large-span tailrace bifurcated tunnels with irregular geometry." *Tunn. Undergr. Sp. Tech.*, Vol. 38, No. 9, pp. 189-204.

Lionco, A. and Assis, A. (2000). "Behaviour of deep shafts in rock considering nonlinear elastic models." *Tunn. Undergr. Sp. Tech.*, Vol. 15, No. 4, pp. 445-451.

Liu, H. H., Rutqvist, J., and Berryman, J. C. (2009). "On the relationship between stress and elastic strain for porous and fractured rock." *Int. J. Rock Mech. Min. Sci.*, Vol. 46, No. 2, pp. 289-296.

Liu, H. H., Rutqvist, J., and Birkholzer, J. T. (2011). "Constitutive relationships for elastic deformation in clay rock: Data analysis." *Rock Mech. Rock Eng.*, Vol. 44, No. 4, pp. 463-468.

Liu, H. Y., Roquete, M., Kou, S. Q., and Lindqvist, P. A. (2004).

"Characterization of rock heterogeneity and numerical verification." *Eng. Geol.*, Vol. 72, Nos. 1-2, pp. 89-119.

Liu, H. H., Wei, M. Y., and Rutqvist, J. (2013). "On the normal-stress dependent fracture properties including two-phase flow properties." *Hydrogeol J.*, Vol. 21, No. 2, pp. 371-382.

Louis, C. (1974). *Rock hydraulics*, In: Muller, L. (Ed.), Rock Mechanics, Springer, Vienna.

Ma, G. W., Wang, X. J., and Ren, F. (2011). "Numerical simulation of compressive failure of heterogeneous rock-like materials using SPH method." *Int. J. Rock Mech. Min. Sci.*, Vol. 48, No. 3, pp. 353-363.

Martin, C. D. and Lanyon, G. W. (2004). *Excavation Disturbed Zone (EDZ) in clay shale: Mont Terri*, Mont Terri Project, Technical Report, TR 2001-01, Mont Terri Rock Laboratory.

Martino, J. B. (2003). *The 2002 international EDZ workshop on the excavation damage zone - causes and effects*, Report 06819-REP-01200-10105-R00, Atomic Energy of Canada Ltd.

Martino, J. B. and Martin, C. D. (1996). *EDZ winnipeg workshop on designing the excavation disturbed zone for a nuclear repository in hard rock*, Canadian Nuclear Society.

Mavko, G. M. and Nur, A. (1978). "The effect of nonelliptical cracks on the compressibility of rocks." *J. Geophys. Res.*, Vol. 83, No. B9, pp. 4459-4468.

McClintock, F. A. and Argon, A. S. (1966). *Mechanical behavior of materials*, Addison-Wesley, Reading, MA.

Minkoff, S. E., Stone, C. M., and Bryant, S. (2003). "Coupled fluid flow and geomechanical deformation modeling." *J. Pet. Sci. Eng.*, Vol. 38, Nos. 1-2, pp. 37-56.

Nawrocki, P. A., Dusseault, M. B., Bratli, R. K., and Xu, G. (1998). "Assessment of some semi-analytical models for non-linear modelling of borehole stresses." *Int. J. Rock Mech. Min. Sci. & Geomech. Abstract*, Vol. 35, No. 4-5, pp. 522-531.

Nur, A. (1971). "Effects of stress on velocity anisotropy in rocks with cracks." *J. Geophys. Res.*, Vol. 76, No. 8, pp. 2022-2034.

Olalla, C., Martin, M., and Saez, J. (1999). *ED-B experiment: Geotechnical laboratory test on Opalinus Clay rock samples*, Technical report TN98-57, Mont Terri Project.

Schulze, O., Popp, T., and Kern, H. (2001). "Development of damage and permeability in deformaing rock salt." *Eng. Geol.*, Vol. 61, No. 2-3, pp.1 63-180.

Pan, P. Z., Feng, X. T., Huang, X. H., Cui, Q., and Zhou, H. (2009). "Coupled THM processes in EDZ of crystalline rocks using an elasto-plastic cellular automaton." *Environ. Geol.*, Vol. 57, No. 6, pp. 1299-1311.

Pan, P. Z., Feng, X. T., and Zhou, H. (2012). "Development and applications of the elasto-plastic cellular automaton." *Acta Mechanica Solida Sinica*, Vol. 25, No. 2, pp. 126-143.

Pearce, C. J., Thavalingam, A., Liao, Z., and Bicanic, N. (2000). "Computational aspects of the discontinuous deformation analysis framework for modeling concrete fracture." *Eng. Fract. Mech.*, Vol. 65, Nos. 2-3, pp. 283-298.

Pietruszczak, S. and Xu, G. (1995). "Brittle response of concrete as a localization problem." *Int. J. Solid. Struct.*, Vol. 32, No. 11, pp. 1517-1533.

Popp, T., Salzer, K., and Minkley, W. (2008). "Influence of bedding planes to EDZ-evolution and the coupled HM properties of Opalinus Clay." *Phys. Chem. Earth*, Vol. 33, Supplement 1, pp. 374-387.

Poulos, H. G. and Davis, E. H. (1974). *Elastic solutions for soil and rock mechanics*, John Wiley and Sons, New York.

Schuster, K., Alheid, H. J., and Boddener, D. (2001). "Seismic investigation of the excavation damaged zone in Opalinus Clay." *Eng. Geol.*, Vol. 61, Nos. 2-3, pp. 189-197.

Shao, J. F., Zhou, H., and Chau, K. T. (2005). "Coupling between anisotropic damage and permeability variation in brittle rocks." *Int. J. Numer. Anal. Meth. Geomech.*, Vol. 29, No. 12, pp. 1231-1247.

Sheldon, H. A. (2009). "Simulation of magmatic and metamorphic fluid production coupled with deformation, fluid flow and heat transport." *Comput. Geosci.*, Vol. 35, No. 11, pp. 2275-2281.

Stormont, J. C. (1997). "In situ gas permeability measurements to delineate damage in rock salt." *Int. J. Rock Mech. Min. Sci.*, Vol. 34, No. 7, pp. 1055-1064.

Stormont, J. C. and Daemen, J. J. K. (1992). "Laboratory study of gas permeability changes in rock salt during deformation." *Int. J. Rock Mech. Min. Sci. & Geomech. Abstr.*, Vol. 29, No. 5, pp. 325-342.

Tang, C. A. and Kou, S. Q. (1998). "Crack propagation and coalescence in brittle materials under compression." *Eng. Fract. Mech.*, Vol. 61, Nos. 3-4, pp. 311-324.

Tang, C. A., Liu, H., Lee, P. K. K., Tsui, Y., and Tham, L. G. (2000). "Numerical studies of the influence of microstructure on rock failure in uniaxial compression—Part I: Effect of heterogeneity." *Int. J. Rock Mech. Min. Sci.*, Vol. 37, No. 4, pp. 555-569.

Tang, C. A., Tham, L. G., Lee, P. K. K., Yang, T. H., and Li, L. C. (2002). "Coupled analysis of Flow, Stress and Damage (FSD) in rock failure." *Int. J. Rock Mech. Min. Sci.*, Vol. 39, No. 4, pp. 477-489.

Tsang, C. F., Jing, L., Stephansson, O., and Kautskz, F. (2005). "The DECOVALEX III project: A summary of activities and lessons learned." *Int. J. Rock. Mech. Min. Sci.*, Vol. 42, Nos. 5-6, pp. 593-610.

Tsang, C. F., Barnichon, J. D., Birkholzer, J., Li, X. L., Liu, H. H., and Sillen X. (2012). "Coupled thermo-hydro-mechanical processes in the near field of a high-level radioactive waste repository in clay formations." *Int. J. Rock. Mech. Min. Sci.*, Vol. 49, No. 1, pp. 31-44.

Vermeer, P. A. and deBorst, R. (1984). "Non-associated plasticity for soils, concrete and rock." *Heron*, Vol. 29, No. 3, pp. 3-64.

Walsh, J. B. (1965). "The effect of cracks on the compressibility of rock." *J. Geophys. Res.*, Vol. 70, No. 2, pp. 381-389.

Wei, M. Y., Liu, H. H., Li, L. C., and Wang, E. Y. (2013). "A fractal-based model for fracture deformation under shearing and compression." *Rock Mech. Rock Eng.*, Vol. 46, No. 6, pp. 1539-1549.

Weibull, W. (1951). "A statistical distribution function of wide applicability." *J. Appl. Mech.*, Vol. 18, No. 6, pp. 293-297.

Weng, M. C., Jeng, F. S., Hsieh, Y. M., and Huang, T. H. (2008). "A simple model for stress-induced anisotropic softening of weak sandstones." *Int. J. Rock. Mech. Min. Sci.*, Vol. 45, No. 2, pp. 155-166.

Wong, T. F., Wong, R. H. C., Chau, K. T., and Tang, C. A. (2006). "Microcrack statistics, Weibull distribution and micromechanical modeling of compressive failure in rock." *Mech. Mater.*, Vol. 38, No. 7, pp. 664-681.

Yang, Y. L. and Aplin, A. C. (2010). "A permeability-porosity relationship for mudstones." *Mar. Pet. Geol.*, Vol. 27, No. 8, pp. 1692-1697.

Yuan, S. C. and Harrison, J. P. (2005). "Development of a hydromechanical local degradation approach and its application to modelling fluid flow during progressive fracturing of heterogeneous rocks." *Int. J. Rock Mech. Min. Sci.*, Vol. 42, Nos. 7-8, pp. 961-984.

Zhang, C. L., Rothfuchs, T., Dittrich, J., and Muller, J. (2008). *Investigations on self-sealing of indurated clay*, GRS Report, GRS-230.

Zhao, Y. and Liu, H. H. (2012). "An elastic strain-stress relationship for porous rock under anisotropic stress conditions." *Rock Mech. Rock Eng.*, Vol. 45, No. 3, pp. 389-399.

Zhu, W. C. and Tang, C. A. (2004). "Micromechanical model for simulating the fracture process of rock." *Rock Mech. Rock Eng.*, Vol. 37, No. 1, pp. 25-56.

Zhu, W. L. and Wong, T. F. (1997). "The transition from brittle faulting to cataclastic flow: Permeability evolution." *J. Geophys. Res.*, Vol. 102, No. B2, pp. 3027-3041.